

Contents lists available at ScienceDirect

Polyhedron

journal homepage: www.elsevier.com/locate/poly



Extending the family of reduced $[Mn_{12}O_{12}(O_2CR)_{16}(H_2O)_x]^{n-}$ complexes, and their sensitivity to environmental factors $^{\text{th}}$



Monica Soler ^{a,1}, Preet Mahalay ^a, Wolfgang Wernsdorfer ^{b,c}, Daphné Lubert-Perquel ^{d,e}, John C. Huffman ^f, Khalil A. Abboud ^a, Stephen Hill ^{d,g}, George Christou ^{a,*}

- ^a Department of Chemistry, University of Florida, Gainesville, FL 32611-7200, USA
- ^b Karlsruher Institut für Technologie (KIT), Physikalisches Institut, Wolfgang-Gaede-Str. 1, 76131 Karlsruhe, Germany
- c Institute of Quantum Materials and Technologies (IQMT), Hermann-von-Helmholtz-Platz 1, Gebäude 640, 76344 Eggenstein-Leopoldshafen, Germany
- ^d National High Magnetic Field Laboratory, Florida State University, Tallahassee, FL 32310, USA
- e Department of Physics, University of Florida, Gainesville, FL 32611-8440, USA
- ^f Molecular Structure Center, Indiana University, Bloomington, IN 47405, USA
- ^g Department of Physics, Florida State University, Tallahassee, FL 32306, USA

ARTICLE INFO

Article history: Received 2 November 2020 Accepted 7 December 2020 Available online 14 December 2020

Keywords: Manganese Clusters Crystal structures Magnetism

ABSTRACT

The family of reduced $[Mn_{12}O_{12}(O_2CR)_{16}(H_2O)_4]^{n-}$ (n = 1, 2) single-molecule magnets (SMMs) has been expanded with the synthesis of new members using I⁻ as a stoichiometric one-electron reducing agent of the neutral n = 0 complexes. Electrochemical data, ¹H NMR spectra of the [Mn₁₂O₁₂(O₂CCH₂Cl)₁₆(H₂O)₃]^{0,-,2-} salts, and the crystal structures of two complexes, (PPh₄) $[Mn_{12}O_{12}(O_2CCHCl_2)_{16}(H_2O)_4] \quad and \quad (PPh_4)_2[Mn_{12}O_{12}(O_2CCH_2Cl)_{16}(H_2O)_3] \quad have \quad been \quad obtained. \quad For \quad (PPh_4)_2[Mn_{12}O_{12}(O_2CCH_2Cl)_{16}(H_2O)_3] \quad have \quad been \quad obtained. \quad For \quad (PPh_4)_2[Mn_{12}O_{12}(O_2CCH_2Cl)_{16}(H_2O)_3] \quad have \quad been \quad obtained. \quad For \quad (PPh_4)_2[Mn_{12}O_{12}(O_2CCH_2Cl)_{16}(H_2O)_3] \quad have \quad been \quad obtained. \quad For \quad (PPh_4)_2[Mn_{12}O_{12}(O_2CCH_2Cl)_{16}(H_2O)_3] \quad have \quad been \quad obtained. \quad For \quad (PPh_4)_2[Mn_{12}O_{12}(O_2CCH_2Cl)_{16}(H_2O)_3] \quad have \quad been \quad obtained. \quad For \quad (PPh_4)_2[Mn_{12}O_{12}(O_2CCH_2Cl)_{16}(H_2O)_3] \quad have \quad been \quad obtained. \quad For \quad (PPh_4)_2[Mn_{12}O_{12}(O_2CCH_2Cl)_{16}(H_2O)_3] \quad have \quad been \quad obtained. \quad For \quad (PPh_4)_2[Mn_{12}O_{12}(O_2CCH_2Cl)_{16}(H_2O)_3] \quad have \quad been \quad obtained. \quad For \quad (PPh_4)_2[Mn_{12}O_{12}(O_2CCH_2Cl)_{16}(H_2O)_3] \quad have \quad (PPH_4)_2[Mn_{12}O_{12}(O_2CCH_2Cl)_{16}(H_2O)_3] \quad (PPH_4)_2[Mn_{12}O_{12}(O_2CCH_2Cl)_{16}(H_2O)_3] \quad have \quad (PPH_4)_2[Mn_{12}O_{12}(O_2CCH_2Cl)_{16}(H_2O)_3] \quad (PPH_4)_2[Mn_{12}O_{12}(O_2CCH_2Cl)_{16}(H_2O)_4] \quad (PPH_4)_2[Mn_{12}O_2CCH_2Cl)_4[Mn_{12}O_2CCH_2Cl)_4[Mn_{12}O_2CCH_2Cl)_4[Mn_{12}O_2CCH_2Cl)_4[Mn_{12}O_2CCH_2Cl)_4[Mn_{12}O_2CCH_2Cl)_4[Mn_$ $(PPh_a)_2[Mn_{12}O_{12}(O_2CCH_2CI)_{16}(H_2O)_3]$, the data confirm an S = 10 ground state, and magnetization vs dc field scans on a pristine crystal exhibit hysteresis loops possessing steps due to quantum tunneling of magnetization (OTM). In addition, two forms of the cluster have been identified in the crystal with distinctly different relaxation barriers, with the faster-relaxing form being the majority one in pristine crystals from mother liquor, and the slower-relaxing one becoming the majority one in vacuum-dried samples. Similar behavior is seen for $(PPh_4)[Mn_{12}O_{12}(O_2CCHCl_2)_{16}(H_2O)_4]$ with an $S = {}^{19}/_2$ ground state, which shows three forms to be present in the hysteresis loops of a pristine crystal, all converting to a slow-relaxing form on vacuum-drying. High-frequency EPR spectra of the latter confirm a high axial anisotropy with D = -0.477 cm⁻¹ and rationalize its effective relaxation barrier $U_{\rm eff} = 57$ K. The combined work emphasizes a high sensitivity of such ultra-small nanomagnets to environmental influences, affecting their properties significantly, especially their quantum properties that are so important to many potential new 21st century applications.

© 2020 Elsevier Ltd. All rights reserved.

1. Introduction

When [Mn₁₂O₁₂(O₂CMe)₁₆(H₂O)₄]·2MeCO₂H·4H₂O (1; 8Mn³⁺, 4Mn⁴⁺) was published by Lis in 1980 [1], it could not have been anticipated how much new chemistry and physics this compound would initiate and how deeply rooted would become the new phenomenon of single-molecule magnets (SMMs). The compound remained little noticed in the literature for over a decade, but it

then opened the door to what subsequently became the deeprooted area of bottom-up nanoscale magnetism that we know today as SMMs [2–5]. Unlike the top-down magnetic nanoparticles of metals, metal oxides, etc, SMMs retain all the advantages of molecular chemistry, including true monodispersity in size and shape, true solubility in common solvents, and crystallinity, the latter allowing structural characterization to atomic resolution by single-crystal X-ray diffractometry. **1** was the first of what soon became the large family of Mn₁₂ clusters that has continued to provide new and interesting results for over a quarter of a century since, even as the SMM field has expanded in so many directions, from Mn clusters of various nuclearities up to Mn₈₄ [6–10] to now encompass a large part of the periodic table [11–13] and span various metal nuclearities and topologies, heterometallic systems [14–16], record breaking breakthroughs into high-temperature

 $^{\,^{\}dot{*}}$ Part of the special issue dedicated to the element manganese, entitled Manganese: A Tribute to Chemical Diversity.

^{*} Corresponding author.

E-mail address: christou@chem.ufl.edu (G. Christou).

¹ Present address: Department of Chemical Engineering, Biotechnology and Materials, FCFM, University of Chile, Beauchef 851, Santiago, Chile.

SMMs [17,18], and fascinating quantum physics previously inaccessible in classical top-down nanomagnets, such as quantum tunneling of magnetization (QTM), discovered originally in 1 [19,20], quantum phase interference [21–23], quantum entanglement [24], and exchange-biased QTM [25–27].

Our group's own work in Mn_{12} chemistry has been extensive, beginning with expanding the family beyond just 1 by developing carboxylate substitution methods to alter the peripheral ligation as desired and thus modify solubilities, redox potentials, space group and molecular symmetries, etc. [28-30]. Among other benefits, this has allowed isolation and study of one-, two-, and three-electron reduced derivatives, expanding the family to four oxidation states $[Mn_{12}O_{12}(O_2CR)_{16}(H_2O)_4]^{n-}$ (n = 0-3). Isolation of the two- and three-electron reduced clusters required good electron-withdrawing carboxylate R groups, and we found the R = CHCl2 cluster a particularly beneficial choice. Comparative study of the structural, magnetic, spectroscopic, and physical properties of the four oxidation states has led to a wealth of fascinating data, such as the discovery in neutral clusters of Jahn-Teller (JT) isomers in which one IT axis is abnormally oriented [31-33], the identification of the metal ions reduced upon electron addition to be the Mn³⁺ not the Mn⁴⁺, the reductions causing a decrease in the magnetic anisotropy and SMM relaxation barrier, and many others [34,35].

Two previous observations of particular relevance to this report are (i) the presence of spin frustration (competing interactions) determining the $[Mn_{12}]^{n-}$ spin ground states and rationalizing the observed S=10, $^{19}/_2$, 10 and $^{17}/_2$ ground states of the n=0, 1-, 2-, and 3- states, respectively, with only a few exceptions, which themselves can be rationalized on the basis of modifications of the spin frustration [36,37], and (ii) the discovery of significantly different SMM relaxation barriers for two crystal forms of $(PPh_4)_2[Mn_{12}O_{12}(O_2CCHCl_2)_{16}(H_2O)_4]$, both with S=10 ground states, and differing only in the solvent of crystallization [34].

A number of $[Mn_{12}O_{12}(O_2CR)_{16}(H_2O)_4]^-$ clusters have been reported with various R groups, and almost all have $S = {}^{19}/_2$ ground states rather than the $S = {}^{21}/{}_2$ expected from the S = 10 spin vector alignments in the neutral clusters, except for a few with $S = {}^{21}/_2$ [36]. This is readily rationalized as due to small changes to the relative magnitudes of the competing exchange interactions [28]. Similarly, $[Mn_{12}O_{12}(O_2CR)_{16}(H_2O)_4]^{2-}$ salts with R = CHCl₂ or C_6F_5 have S = 10 whereas the polycationic cluster with betaine as the carboxylate is S = 11 [37]. Such variations in the ground states are very interesting and, particularly for the few $[Mn_{12}]^{2-}$ clusters that are currently known, we wondered what S ground states would result from less electron-withdrawing R groups than CHCl₂ and C₆F₅. Over the years we have prepared a number of other [Mn₁₂]ⁿ⁻ clusters, and we have collected their syntheses here together with two crystal structures of the $[Mn_{12}]^-/R = CHCl_2$ and $[Mn_{12}]^{2-}/R = CH_2Cl$ analogues, and magnetic and spectroscopic properties. We herein describe these results which have also revealed additional examples of a fascinating sensitivity of these reduced [Mn₁₂]ⁿ⁻ clusters to environmental influences of the solvent of crystallization.

2. Experimental

2.1. Compounds

For convenience, the compounds described in this paper are listed below:

```
 \begin{split} & [Mn_{12}O_{12}(O_2CMe)_{16}(H_2O)_4] \cdot 2MeCO_2H \cdot 4H_2O \ (\textbf{1}) \\ & [Mn_{12}O_{12}(O_2CCHCl_2)_{16}(H_2O)_4] \ (\textbf{2}) \\ & [Mn_{12}O_{12}(O_2CCH_2Cl)_{16}(H_2O)_4] \ (\textbf{3}) \\ & [Mn_{12}O_{12}(O_2CC_6H_3-2,4-(NO_2)_2)_{16}(H_2O)_4] \ (\textbf{4}) \end{split}
```

```
 \begin{array}{l} (PPh_4)[Mn_{12}O_{12}(O_2CCHCl_2)_{16}(H_2O)_4] \  \, \textbf{(5)} \\ (PPh_4)[Mn_{12}O_{12}(O_2CCH_2Cl)_{16}(H_2O)_4] \  \, \textbf{(6)} \\ (PPh_4)[Mn_{12}O_{12}(O_2CC_6H_3-2,4-(NO_2)_2)_{16}(H_2O)_4] \  \, \textbf{(7)} \\ (PPh_4)_2[Mn_{12}O_{12}(O_2CCH_2Cl)_{16}(H_2O)_3] \  \, \textbf{(8)} \\ (PPh_4)_2[Mn_{12}O_{12}(O_2CC_6H_3-2,4-(NO_2)_2)_{16}(H_2O)_4] \  \, \textbf{(9)} \\ (PPh_4)_2[Mn_{12}O_{12}(O_2CCHCl_2)_{16}(H_2O)_4] \  \, \textbf{(10)} \\ (NMe_4)_2[Mn_{12}O_{12}(O_2CC_6F_5)_{16}(H_2O)_4] \  \, \textbf{(11)} \end{array}
```

2.2. Syntheses

All preparations were performed under aerobic conditions using chemicals as received. Complex 1 was prepared as described elsewhere [1]. Complexes 2, 3 and 4 were prepared from 1 as described in detail elsewhere for 2 [38,39]. 5 was prepared as reported previously except that the mixture was heated to 50 °C [33].

2.2.1. $(PPh_4)[Mn_{12}O_{12}(O_2CCH_2Cl)_{16}(H_2O)_4]$ (**6**)

Complex **3** (0.40 g, 0.165 mmol) and PPh₄I (0.077 g, 0.165 mmol) were dissolved in MeCN (50 mL) and stirred for 4 h. The generated I_2 was removed by extraction with hexanes (6 \times 25 mL) and the MeCN then removed by rotary evaporation under vacuum until dry. The residue was recrystallized from CH₂Cl₂/hexanes, and the resulting black crystals were collected by filtration, washed with hexanes and dried under vacuum; the yield was 65%. *Anal.* Calc. (Found) for **6**·H₂O (C₅₆H₆₂Mn₁₂O₄₉Cl₁₆P): C, 24.22 (24.03); H, 2.25 (2.52) %.

2.2.2. $(PPh_4)[Mn_{12}O_{12}(O_2CC_6H_3-2,4-(NO_2)_2)_{16}(H_2O)_4]$ (7)

Complex **7** was prepared using the same procedure as for **6** but with $[Mn_{12}O_{12}(O_2CC_6H_3-2,4-(NO_2)_2)_{16}(H_2O)_4]$ (**4**) (0.71 g, 0.165 mmol). The yield was 55%. *Anal.* Calc. (Found) for **7** ($C_{136}H_{76}-Mn_{12}O_{112}N_{32}P$): C, 35.20 (35.01); H, 1.65 (1.76); N, 9.66 (9.62) %.

2.2.3. $(PPh_4)_2[Mn_{12}O_{12}(O_2CCH_2Cl)_{16}(H_2O)_3]$ (8)

Complex **3** (0.40 g, 0.165 mmol) and PPh₄I (0.154 g, 0.331 mmol) were dissolved in MeCN (50 mL) and stirred for 4 h. The generated I₂ was removed by extraction with hexanes (6 \times 25 mL) and the solvent then removed by rotary evaporation under vacuum until dry. The residue was recrystallized from CH₂Cl₂/hexanes, and the resulting black crystals of **8**·5CH₂Cl₂·H₂O were collected by filtration, washed with hexanes and dried under vacuum; the yield was 65%. *Anal.* Calc. (Found) for **8**·2H₂O (C₈₀H₈₂Mn₁₂O₄₉Cl₁₆P₂): C, 30.84 (30.64); H, 2.65 (2.72) %. The crystallographic sample was not filtered but instead maintained in mother liquor to avoid solvent loss and degradation of its crystallinity.

2.2.4. $(PPh_4)_2[Mn_{12}O_{12}(O_2CC_6H_3-2,4-(NO_2)_2)_{16}(H_2O)_4]$ (9)

Complex **9** was prepared using the same procedure as for **8** but with $[Mn_{12}O_{12}(O_2CC_6H_3-2,4-(NO_2)_2)_{16}(H_2O)_4]$ (**4**) (0.71 g, 0.165 mmol); the yield was 75%. *Anal.* Calc. (Found) for **9**·2H₂O (C₁₆₀H₁₀₀Mn₁₂O₁₁₄N₃₂P₂): C, 38.31 (38.76); H, 2.01 (2.07); N, 8.94 (8.48) %.

2.3. X-ray crystallography

Suitable single crystals of $5 \cdot x(solv)$ and $8 \cdot 5 \cdot CH_2Cl_2 \cdot H_2O$ were attached to glass fibers using silicone grease and transferred to the goniostat where they were cooled to 100 and 135 K, respectively, for characterization and data collection.

For $\mathbf{5} \cdot \mathbf{x}(\text{solv})$, data were collected on a Bruker DV8 Venture diffractometer using MoK_{α} radiation ($\lambda = 0.71073 \text{ Å}$) and a Photon III area detector. Raw data frames were read by program SAINT [40] and integrated using 3D profiling algorithms. The resulting data were reduced to produce hkl reflections and their intensities

and estimated standard deviations. The data were corrected for Lorentz and polarization effects and numerical absorption corrections were applied based on indexed and measured faces. The structure was solved and refined in SHELXTL2014, using full-matrix least-squares cycles [40,41]. The non-H atoms were refined with anisotropic thermal parameters, and all H atoms were placed in calculated idealized positions and refined riding on their parent atoms. For 8.5CH2Cl2·H2O, data were collected on a Bruker Platform goniometer equipped with a SMART 6000 CCD detector. Examination of a limited portion of reciprocal space indicated the centrosymmetric space group P1. Data were collected using 30 s frames with an omega scan of 0.3°. Data were corrected for Lorentz and polarization effects and equivalent reflections averaged using the Bruker SAINT [40] software and utility programs from the XTEL library. An absorption correction was performed using the SADABS program. The structure was solved using SHELXTL and Fourier techniques, and refined by full-matrix least-squares cycles. The non-H atoms were refined with anisotropic thermal parameters, and all H atoms were placed in calculated idealized positions and refined riding on their parent atoms.

For **5**·x(solv), the asymmetric unit consists of a $^{1}/_{8}$ [Mn₁₂]⁻ cluster anion located on a 42m symmetry position, a PPh₄⁺ cation located on a 3m symmetry position, and disordered solvent comprising a volume of 7787 Å³ and 1881 electrons in the unit cell. The solvent (CH2Cl2 and/or hexanes) was too disordered to be modelled properly, and program SQUEEZE [42], a part of the PLA-TON package of crystallographic software [43], was therefore used to calculate the solvent disorder area and remove its contribution to the overall intensity data. The CHCl₂CO₂ ligands on the Mn₁₂ equatorial plane are not disordered, but four axial carboxylate (C11) ligands are each disordered by the mirror planes with a water ligand. Similarly, the four other axial carboxylate (C21) ligands are disordered by mirror planes but only their -CHCl2 groups. The PPh₄⁺ cation is located on a 3m symmetry site with three Ph rings disordered in two parts and the apical Ph ring disordered over six positions. In the final cycle of refinement, 4624 reflections (of which 3372 are observed with $I > 2\sigma(I)$) were used to refine 204 parameters and the resulting R_1 , wR_2 and S (goodness of fit) were 4.77%, 11.79% and 1.024, respectively.

For complex $8.5 \text{CH}_2\text{Cl}_2 \cdot \text{H}_2\text{O}$, the asymmetric unit consists of the complete $[\text{Mn}_{12}]^{2-}$ dianion and two PPh₄ cations, in addition to five independent CH_2Cl_2 and one H_2O solvent molecules. There is some disorder present in the Cl atom of one $\text{ClH}_2\text{CO}_2^-$ ligand, and in one CH_2Cl_2 solvent molecule. There are only three H_2O ligands on the $[\text{Mn}_{12}]^{2-}$ dianion, thus Mn10 is five-coordinate, and the lattice H_2O molecule (O108) is hydrogen-bonding to two O atoms within the dianion, water ligand O25 and central oxide ion O13. The final difference Fourier map was essentially featureless, with all peaks over $1\text{e}/\text{Å}^3$ in the vicinity of disordered atoms. In the final cycle of refinement, 48,443 reflections (of which 28,747 are observed with $I > 2\sigma(I)$) were used to refine 9927 parameters and the resulting R_1 , wR₂ and S (goodness of fit) were 5.31%, 13.33% and 0.99, respectively. Crystal data and structure refinement parameters for both complexes are listed in Table 1.

2.4. Physical measurements

Elemental analyses (C, H, N) were performed by Atlantic Microlab in Norcross, Georgia, USA. ¹H NMR spectra were obtained at 300 MHz on a Varian XL-300 spectrometer, using protio-solvent signals as internal references. Electrochemical studies were carried out on a BASi model CV-50W voltammetric analyzer using a standard three-electrode set-up: glassy carbon working electrode, Pt wire auxiliary, and Ag/AgNO₃ reference electrode. No IR compensation was employed. Quoted potentials are vs the ferrocene/ferrice-

Table 1
Crystallographic and structure refinement data for complexes 5 and 8.

	5·x(solv)	8 ⋅5CH ₂ Cl ₂ ⋅H ₂ O
Formula	C ₅₆ H ₃₆ Cl ₃₂ Mn ₁₂ O ₄₈ P ^a	$C_{85}H_{90}Cl_{26}Mn_{12}O_{48}P_2^{\ b}$
$FW (g mol^{-1})^a$	3301.50	3522.45
Space group	<i>I</i> 43m	$P\overline{1}$
a (Å)	29.190(6)	13.3878(8)
b (Å)	29.190(6)	21.5581(13)
c (Å)	29.190(6)	24.5398(15)
α (°)	90	70.295(1)
β (°)	90	79.008(1)
γ (°)	90	72.214(1)
$V(Å^3)$	24872(15)	6318.7(7)
Z	6	2
T (K)	100(2)	135(2)
λ (Å)	0.71073	0.71073
$ ho_{ m Calc}$ (g cm $^{-3}$)	1.323	1.848
$R_1^{\mathrm{b,c}}$	0.0477	0.0531
$wR_2^{ m d}$	0.1179	0.1333

^a Excluding solvent molecules. ^b Including solvent molecules.

nium couple, used as an internal standard. Measurements were performed on solutions containing 1 mM analyte and 0.1 M NBuⁿ₄-PF₆ as supporting electrolyte in distilled and degassed MeCN. Variable-temperature dc and ac magnetic susceptibility data were collected at the University of Florida using a Quantum Design MPMS-XL SQUID magnetometer equipped with a 7 T magnet and operating in the 1.8-300 K range. Samples were embedded in solid eicosane to prevent torquing. Magnetization versus field and temperature data were fit using the program MAGNET [44]. Pascal's constants were used to estimate the diamagnetic correction [45], which were subtracted from the experimental susceptibility to give the molar paramagnetic susceptibility (χ_M). Low-temperature (<1.8 K) hysteresis loop and dc relaxation measurements were performed at CNRS, Grenoble, France, using an array of micro-SQUIDs [46]. The high sensitivity of this magnetometer allows the study of single crystals of SMMs of the order of 10 to 500 μm . The field can be applied in any direction by separately driving three orthogonal coils. High-field EPR (HFEPR) spectra were collected on a vacuumdried microcrystalline powder sample of $5^{-3}/_2$ hexane. The transmission-type spectrometer used in this study employed a 17 T superconducting magnet (Oxford Instruments) in conjunction with a phase locked microwave source combined with a series of Schottky diode multipliers (Virginia Diodes, Inc.), providing frequencies in the 50 to ~500 GHz range [47]. Detection of the field modulated derivative mode signal, dI/dB (I is the microwave intensity transmitted through the sample and B the applied magnetic field), was achieved using an InSb hot-electron bolometer (QMC Ltd.) and a lock-in amplifier. Temperature control was accomplished using a continuous helium flow cryostat (Oxford Instruments).

3. Results and discussion

3.1. Syntheses

The neutral Mn_{12} clusters **2**, **3**, and **4** were synthesized from **1** using the carboxylate substitution methodology we have reported previously [34,38]. This involves treatment of **1** with an excess of a second carboxylic acid RCO₂H. The resulting equilibrium (Eq. 1) must be driven

$$\begin{split} [\mathsf{M} n_{12} \mathsf{O}_{12} (\mathsf{O}_2 \mathsf{CMe})_{16} (\mathsf{H}_2 \mathsf{O})_4] \; + \; & 16 \; \mathsf{RCO}_2 \mathsf{H} \; \rightleftharpoons \; [\mathsf{M} n_{12} \mathsf{O}_{12} (\mathsf{O}_2 \mathsf{CMe})_{16-x} \\ & (\mathsf{O}_2 \mathsf{CR})_x (\mathsf{H}_2 \mathsf{O})_4] \; + \; x \mathsf{MeCO}_2 \mathsf{H} + (16-x) \mathsf{RCO}_2 \mathsf{H} \end{split} \tag{1}$$

b $I > 2\sigma(I)$.

 $^{^{}c}R_{1} = \Sigma(||Fo| - |Fc||) / \Sigma|Fo|.$

 $^{^{}d} wR_{2} = \left[\sum [w(Fo^{2} - Fc^{2})^{2}] / \sum [w(Fo^{2})^{2}] \right]^{1/2}.$

to completion, either by repeated treatment of $\mathbf{1}$ with an excess of RCO₂H with a lower pK_a than acetic acid or, more generally useful, removal of the generated acetic acid under vacuum as its toluene azeotrope. These conditions have allowed a variety of Mn₁₂ derivatives to be obtained in pure form differing only in their carboxylate ligation [28]. The preparation of $\mathbf{2}$ by the azeotrope method was reported in detail previously [38], and the same method was found to work very well for $\mathbf{3}$ and $\mathbf{4}$.

3.2. Electrochemical studies

The electrochemical properties of the R = $CHCl_2(2)$ and R = C_6F_5 derivatives have been described elsewhere and they showed that these electron-withdrawing ligands lead to multiple reversible reductions being observed [34,35]. This formed the basis for our initial studies of how the properties of the Mn₁₂ SMMs vary with oxidation state as the clusters are progressively reduced [28,39]. We were thus interested to compare them with the properties of 3 and 4. The cyclic voltammogram (CV) and differential pulse volammogram (DPV) for 4 (Fig. 1) reveal three quasi-reversible reductions and evidence for a fourth irreversible reduction. This is very similar to that previously seen for 2 (Fig. S1) except for the difference in reduction potentials. The latter for the first two reductions of 3 and 4 are compared with those for 2 in Fig. 2, and the observed order of 2 > 4 > 3 in ease of reduction correlates with the relative electron-withdrawing ability Cl₂HC > $2,4-(NO_2)_2C_6H_3 > ClH_2C$, as reflected in the pK_a values of the corresponding acids of 1.26, 1.43, and 2.87, respectively [48]. The reduction potentials for 3 and 4 are still at relatively high values and so we decided to pursue the generation and isolation of the one- and two-electron reduced derivatives. We did not pursue three-electron reduction since previous work with 2 had established the limited stability in solution of the [Mn₁₂]³⁻ anion at greater timescales [34]. Note that a two-electron reduced $[Mn_{12}]^{2-}$ cluster which is overall polycationic has also been reported [49] and that, in the solid-state, a 'super-reduced' Mn₁₂ has been reported to be generated in solid-state electrochemical studies [50].

3.3. Synthesis of reduced $[Mn_{12}]^{-,2-}$ clusters

The high reduction potentials made I⁻ a convenient reducing agent for our purposes, and the one-electron reduced derivatives, **5**, **6**, and **7** were successfully synthesized by treating the neutral complexes with one equivalent of PPh₄I in MeCN. Similarly, the two-electron reduced derivatives, **8** and **9**, were prepared by treatment with two equivalents of PPh₄I (Eq. 2). The addition of the

reducing agent resulted in little apparent color change, but the formation of I_2 was confirmed by its extraction into a hexane phase, which also ensured that the equilibrium was driven to completion. Removal of MeCN under vacuum and recrystallization from $CH_2CI_2/$ hexanes gave black crystalline materials in good yield (\geq 60%) and analytical purity. Several iodide salts have previously been employed in such reductions, such as NPr^n_4I [51], but here we employed the PPh_4^+ cation which tends to give good crystals suitable for X-ray studies and sufficient solubility for spectroscopic studies.

3.4. Description of structures

The structure of the monoanion of **5** is shown in Fig. 3 and has the standard topology of the Mn_{12} family, comprising a central $\{Mn_4O_4\}$ cubane held within a non-planar $\{Mn_8O_8\}$ loop, with peripheral ligation provided by sixteen bridging $CHCl_2CO_2^-$ and

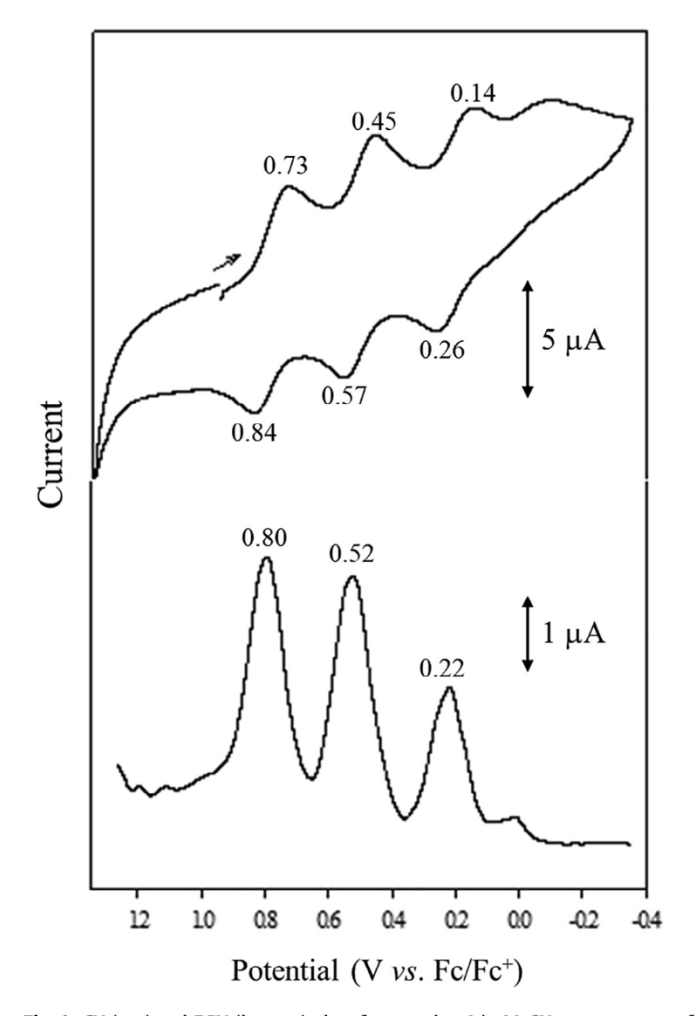


Fig. 1. CV (top) and DPV (bottom) plots for complex ${\bf 4}$ in MeCN at a scan rate of 100 mV/s.

terminal water ligands. However, since 5 crystallizes in a high symmetry space group (143 m) and lies on a site of crystallographic D_{2d} symmetry even though the cluster only has virtual D_2 symmetry (in fact, less if the localized Mn2+ generated by reduction is included), there is disorder of the axial ligands owing to the crystallographic mirror planes. Thus, four axial carboxylates are each wholly disordered with a neighboring water ligand (Fig. S2), but the other four are disordered only in their R groups. Also as a result of the crystallographic symmetry, the location of the Mn²⁺ generated by the one-electron reduction is statistically disordered about the four Mn positions, but on the basis of crystal structures of previous $[Mn_{12}]^{-,2-}$ structures, including that of the $[Mn_{12}]^{2-}$ complex 10 with CHCl₂CO₂ ligands [34], the Mn²⁺ is at atom Mn3 and its symmetry partners. Mn bond valence sum (BVS) calculations [52] (Table S1) confirm Mn1 to be MnIV, and the lower BVS for Mn3 vs Mn2 is taken as support that the Mn²⁺ position is disordered about the former site. The Mn3+ JT axes are all in the 'normal' orientation, i.e., roughly perpendicular to the {Mn₁₂O₁₂} plane, and thus avoiding the short Mn^{III}-O²⁻ bonds [33.34].

The structure of the dianion of $\bf 8$ is shown in Fig. 4, and selected interatomic distances are listed in Table S2. This complex crystallizes in a general position in triclinic space group $P\bar{\bf 1}$, so there are no complications from crystallographically-imposed disorder. The structure is very similar to that of the anion of $\bf 5$ except that the two Mn²⁺ ions formed from the two-electron reduction are clearly

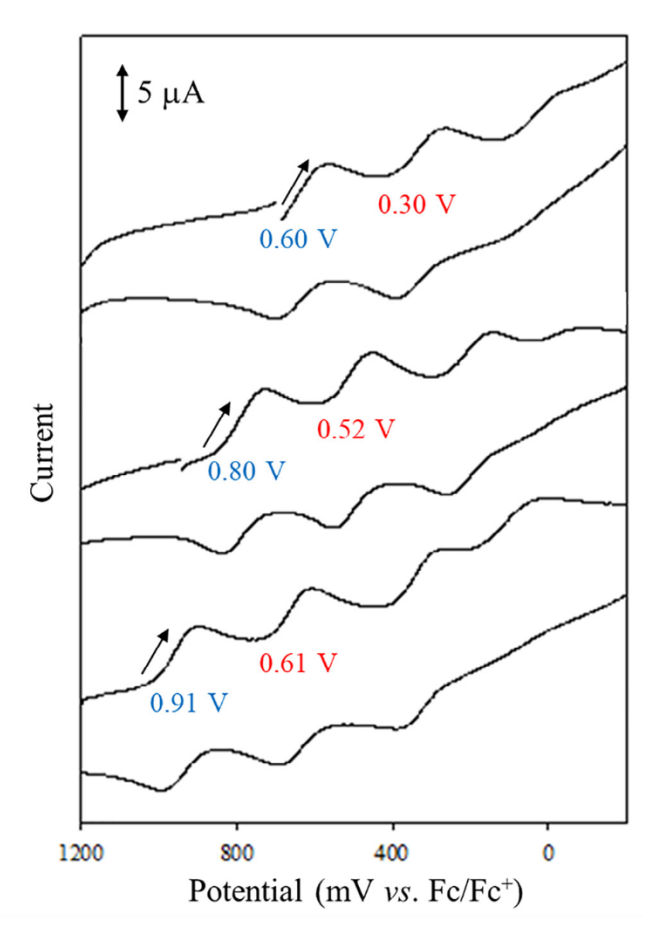


Fig. 2. CV profiles for complexes **3** (a), **4** (b), and **2** (c). $E_{1/2}$ potentials are those obtained from DPV peak positions and are vs. Fc/Fc^+ : 1st reduction potential, blue; 2nd reduction potential, red.

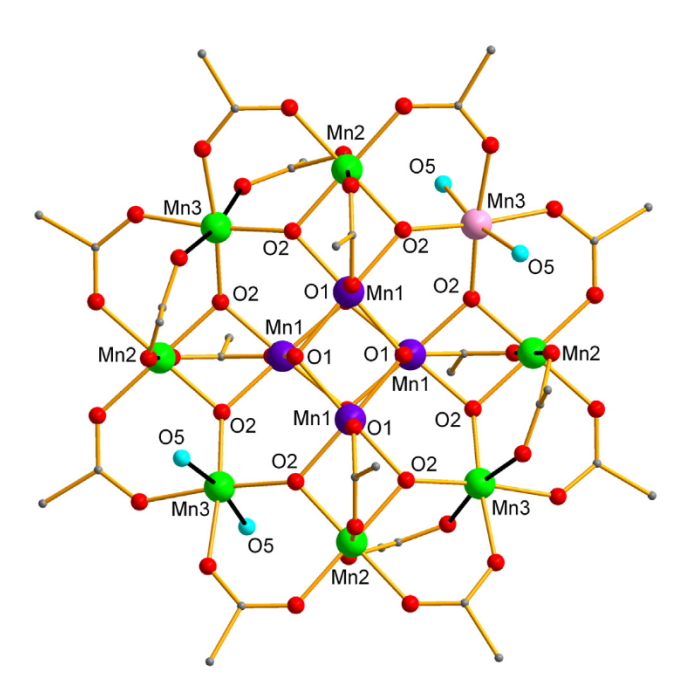


Fig. 3. Partially labeled structure of the anion of **5.** For clarity, the carboxylate Cl atoms and all H atoms have been omitted, and only one disorder position of the Mn²⁺ and the ligands is shown. Mn³⁺ JT axes are shown as black bonds. Color code: Mn⁴⁺ purple, Mn³⁺ green, Mn²⁺ pink, O red, H₂O sky-blue, C gray.

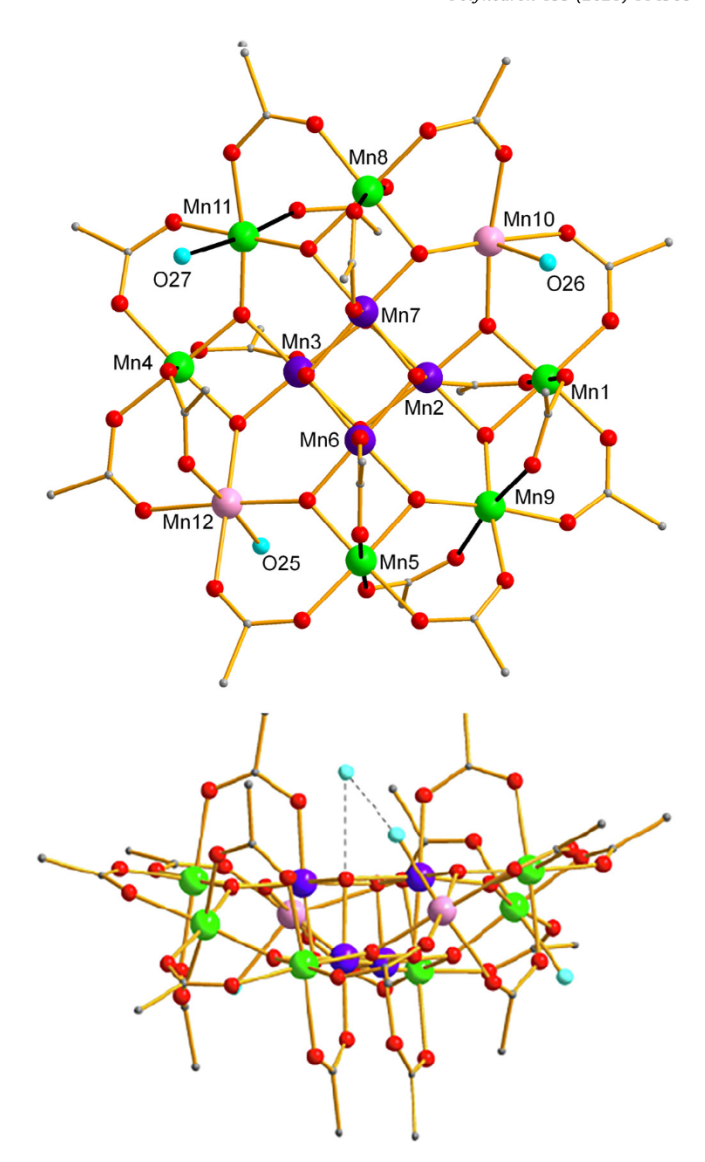


Fig. 4. (top) Partially labeled structure of the dianion of **8**, and (bottom) a side view also including the water molecule hydrogen-bonding with the core. For clarity, the carboxylate Cl atoms and all H atoms have been omitted. Mn³⁺ JT axes are shown as black bonds. Color code: Mn⁴⁺ purple, Mn³⁺ green, Mn²⁺ pink, O red, H₂O sky-blue, C, gray.

identified as Mn10 and Mn12. This was concluded from the metric parameters and the BVS calculations (Table S1). Peripheral ligation is by sixteen bridging $CH_2CICO_2^-$ and only three terminal H_2O groups, the latter bound to Mn10, Mn11 and Mn12. Another H_2O molecule (O108) is nearby but not bound – instead it is hydrogen-bonded to water O25 and oxide O13 of the central cubane, with O108...O25 = 2.782(6) Å and O108...O13 = 2.872(6) Å (Fig. 4). Mn10 is thus five-coordinate with near-ideal square pyramidal geometry: τ_5 = 0.04, where τ = 0 and 1 for perfect square pyramidal and trigonal bipyramidal geometry, respectively [53,54,55]. The Mn³+ JT axes are again all in the 'normal' orientation avoiding the short Mn^{III}-O²- bonds (Table S2).

Complexes **5** and **8** are the eighth and fourth examples of structurally characterized $[Mn_{12}]^-$ and $[Mn_{12}]^{2-}$ clusters, respectively. In general, their structural features, where clearly visible, support the trends deduced from previous studies of $[Mn_{12}]^{n-}$ species: (i) Reduction takes place at the outer Mn^{3+} rather than the central Mn^{4+} positions leading to $[Mn_{12}]^{n-}$ products with three Mn oxidation states, nMn^{2+} , $(8-n)Mn^{3+}$, $4Mn^{4+}$ [30,49]; (ii) two-electron reduced clusters always have the resulting Mn^{2+} ions on opposite

sides of the anion, *trans* to the central cubane, presumably to minimize Mn^{3+} electrostatic repulsions; and (iii) "JT isomerism", i.e., one or more JT elongation axes in 'abnormal' positions in the $\{Mn_{12}O_{12}\}$ plane and thus elongating $Mn^{3+}-O^{2-}$ bonds, have never been identified in anionic $[Mn_{12}]^{n-}$ species. Note that clusters containing three Mn oxidation states are quite rare with only a few examples outside the $[Mn_{12}]^{n-}$ family [56,57]. The presence of only three coordinated water molecules in the anion of $\bf 8$ is also rare but not unprecedented, having first been seen in neutral $[Mn_{12}O_{12}(O_2-CEt)_{16}(H_2O)_3]$ [30]. There is even a Mn_{12} complex with no H_2O ligands, $[Mn_{12}O_{12}(O_2CMe)_{12}(O_2P(OPh)_2)_4]$ induced by the presence of bulky $(PhO)_2PO_2^-$ ligands [58]. The possibility of JT isomerism in $[Mn_{12}]^{n-}$ species is further addressed below.

3.5. ¹H NMR spectroscopy

To explore the structure and stability in solution, ¹H NMR studies were carried out on the representative [Mn₁₂O₁₂(O₂CCH₂Cl)₁₆ $(H_2O)_4]^{0,-,2-}$ family, i.e., complexes **3**, **6** and **8** to complement prior ¹H NMR and ¹⁹F NMR spectral studies [34,35]. Neutral Mn₁₂ complexes with S_4 or D_2 virtual symmetry in the solid state, which gives four symmetry-inequivalent sets of four carboxylates, predicts four NMR peaks in a 1:1:1:1 ratio, two axial and two equatorial. However, the obtained spectra from several previous studies are consistent with a higher symmetry in solution. For example, the parent complex $[Mn_{12}O_{12}(O_2CCH_3)_{16}(H_2O)_4]$ (1) in CD₃CN exhibits only three paramagnetically-shifted acetate peaks at δ = 13.9, 41.8 and 48.2 ppm in a 1:2:1 integration ratio. The spectra of many other neutral Mn₁₂ complexes show the same 1:2:1 pattern, showing that it is not just resulting from a coincidental superposition of two of the peaks in 1. Instead, the solution spectra are reflecting effective D_{2d} symmetry, under which all the equatorial acetates, for example, are equivalent. Variable-temperature studies of various Mn₁₂ complexes have established a fluxional process to be exchanging the axial water molecules with adjacent carboxylate groups rapidly on the NMR timescale at room temperature, which serves to introduce vertical (dihedral) mirror planes onto the molecule. The net effect is thus akin to that in Fig. S2, except that there it is due to static disorder about the crystallographic mirror planes, not a dynamic process.

The obtained 1H NMR spectra for **3**, **6** and **8** in CD₂Cl₂ are shown in Fig. 5. The spectrum for the neutral Mn₁₂ complex (Fig. 5, bottom) displays four resonances in a 1:1:1:1 ratio. This might at first seem inconsistent with the discussion above predicting a 1:2:1 ratio, but it is not – it is due to the fact that the two H₂C– hydrogen atoms of the equatorial carboxylates are not related by any symmetry operation and are thus diastereotopic, giving separate signals and a resulting 1:1:1:1 ratio of four resonances; the H₂C–hydrogen atoms of the axial ligands are equivalent due to the effective mirror planes. The same situation is seen for the H₂C hydrogen atoms in the 1H NMR spectrum of [Mn₁₂O₁₂(O₂CEt)₁₆(H₂O)₃] [30].

For the $[Mn_{12}]^-$ (6) and $[Mn_{12}]^{2-}$ (8) complexes (Fig. 5, middle and top, respectively), the pattern remains the same, except for small shifts in the resonance positions and the appearance of the cation as an intense resonance at ~ 8 ppm. This is consistent again with D_{2d} solution symmetry owing to the fluxional process and the added electrons being detrapped on the 1H NMR timescale around the outer ring of the Mn_{12} complex. Chemical shifts and T_1 times for 1, 3, 6 and 8 are listed in Table 2. The overall behavior is thus analogous to that observed for the $CHCl_2CO_2^-$ family, 2, 5 and 10 [34].

3.6. SQUID magnetochemistry

Solid-state, variable-temperature dc magnetic susceptibility data in the 5.0–300 K range were collected on crushed microcrys-

talline samples of vacuum-dried **8**·2H₂O restrained in eicosane to prevent torquing. The $\chi_{\rm M}T$ value slowly increases from 21.89 cm³Kmol⁻¹ at 300 K to a maximum of 44.76 cm³Kmol⁻¹ at 15.0 K (Fig. S3) and then decreases below this temperature. To determine the ground state, magnetization (M) data were collected in the 10–70 kG and 1.80–4.00 K ranges and are plotted as reduced magnetization ($M/N\mu_B$) vs. H/T in Fig. 6, where N is Avogadro's number and μ_B is the Bohr magneton. The data were fit using MAGNET [44], which assumes only the ground state is populated at these temperatures and incorporates axial zero-field splitting (zfs), Zeeman interactions, and a full powder average. The corresponding spin Hamiltonian is given by Eq. (3), where \hat{S} is the electron spin operator and \hat{S}_z its projection onto the z-axis, D is the axial zfs parameter, g is the electronic g factor, and μ_0 is the vacuum

$$\widehat{H} = D\widehat{S}_z^2 + g\mu_B\mu_0\widehat{S} \cdot H \tag{3}$$

permeability; the first term describes the axial zfs interaction and the last term is the Zeeman energy associated with the applied magnetic field. The best fit (solid lines in Fig. 6) gave S=10, $D=-0.26~{\rm cm}^{-1}=-0.37~{\rm K}$ and g=1.94. The data can also be fit for S=11 giving $D=-0.21~{\rm cm}^{-1}=-0.30~{\rm K}$ and g=1.76, which was rejected due to the very low g value. The S=10 ground state spin is thus the same as found for the $[{\rm Mn}_{12}]^{2-}$ clusters with $R={\rm CHCl}_2$ [34] and C_6F_5 [35] reported previously. Similarly, the D is similar to the -0.28 and $-0.29~{\rm cm}^{-1}$, respectively, found for the latter two compounds. The S/D values for the three oxidation levels of $\bf 3$, $\bf 6$ and $\bf 8$ are: ${\rm Mn}_{12}$, $10/-0.44~{\rm cm}^{-1}$; $[{\rm Mn}_{12}]^{1-}$, $^{19}/_2/-0.35~{\rm cm}^{-1}$; $[{\rm Mn}_{12}]^{2-}$, $10/-0.26~{\rm cm}^{-1}$, respectively.

Ac magnetic susceptibility studies in zero dc field and a 3.5 G ac field were carried out on 8.2H₂O in the 1.8 - 10 K range and the data are shown in Fig. 7. The ac in-phase $\chi'_{M}T$ vs. T shows a plateau value at 53 cm³Kmol⁻¹ down to ~6 K confirming a well isolated S = 10 ground state with g slightly less than 2.0 (spin-only values for S = 9, 10 and 11 are 45, 55, and 66 cm³Kmol⁻¹, respectively), in agreement with the dc magnetization fit. Below 6 K, there is a frequency-dependent drop due to blocking of magnetization relaxation, concomitant with the appearance of an ac out-of-phase (χ''_{M}) signal with peaks in the 2–3 K range. This is within the range where χ''_{M} peaks for other $[Mn_{12}]^{2-}$ clusters have been observed. Typical ranges are 6-8 K, 4-6 K, and 2-4 K for Mn_{12} , $[Mn_{12}]^{1-}$, and $[Mn_{12}]^{2-}$, respectively; the χ''_{M} vs T plots for **3**, **6**, and 8.2H₂O are shown in Fig. 8. The smaller peaks at 2–3 K for neutral 3 in Fig. 8a are due to a small component of the 'faster-relaxing' IT isomer with an abnormally oriented [T axis [31,32,33,59]. The $[Mn_{12}]^-$ 6 in Fig. 8b shows a less pronounced feature at ~2 K that may also be due to a JT isomer, but any such second component for the $[Mn_{12}]^{2-}$ 8-2H₂O in Fig. 8c would be below the operating limit of our SQUID instrument (1.8 K). Using the peak positions at various frequencies for 8.2H₂O and the methods described elsewhere [28] allows an Arrhenius plot to be constructed, based on Eq. 4, from

$$(1/\tau) = (1/\tau_0) \exp(-U_{\text{eff}}/kT)$$
 (4)

which were obtained $U_{\rm eff}$ = 33 K and τ_0 = 2.2 × 10⁻⁹ s, where $U_{\rm eff}$ is the effective anisotropy energy barrier, k is the Boltzmann constant, and $1/\tau_0$ is the pre-exponential factor. These values are similar to those for other $[{\rm Mn}_{12}]^{2-}$ salts, as summarized in Table 3.

For reasons to be described below (vide infra), we also ran the $\chi''_{\rm M}$ vs T plots for ${\bf 8}\cdot {\rm SCH_2Cl_2\cdot H_2O}$ crystals freshly removed from mother liquor, dabbed dry with tissue, and quickly enveloped in eicosane. The resulting plot (Fig. 9) showed distinct differences with the vacuum-dried ${\bf 8}\cdot {\rm 2H_2O}$ (Fig. 8c), with the $\chi''_{\rm M}$ peaks shifted to lower temperatures and exhibiting a shoulder in the 3–5 K range suggesting the presence of a second species.

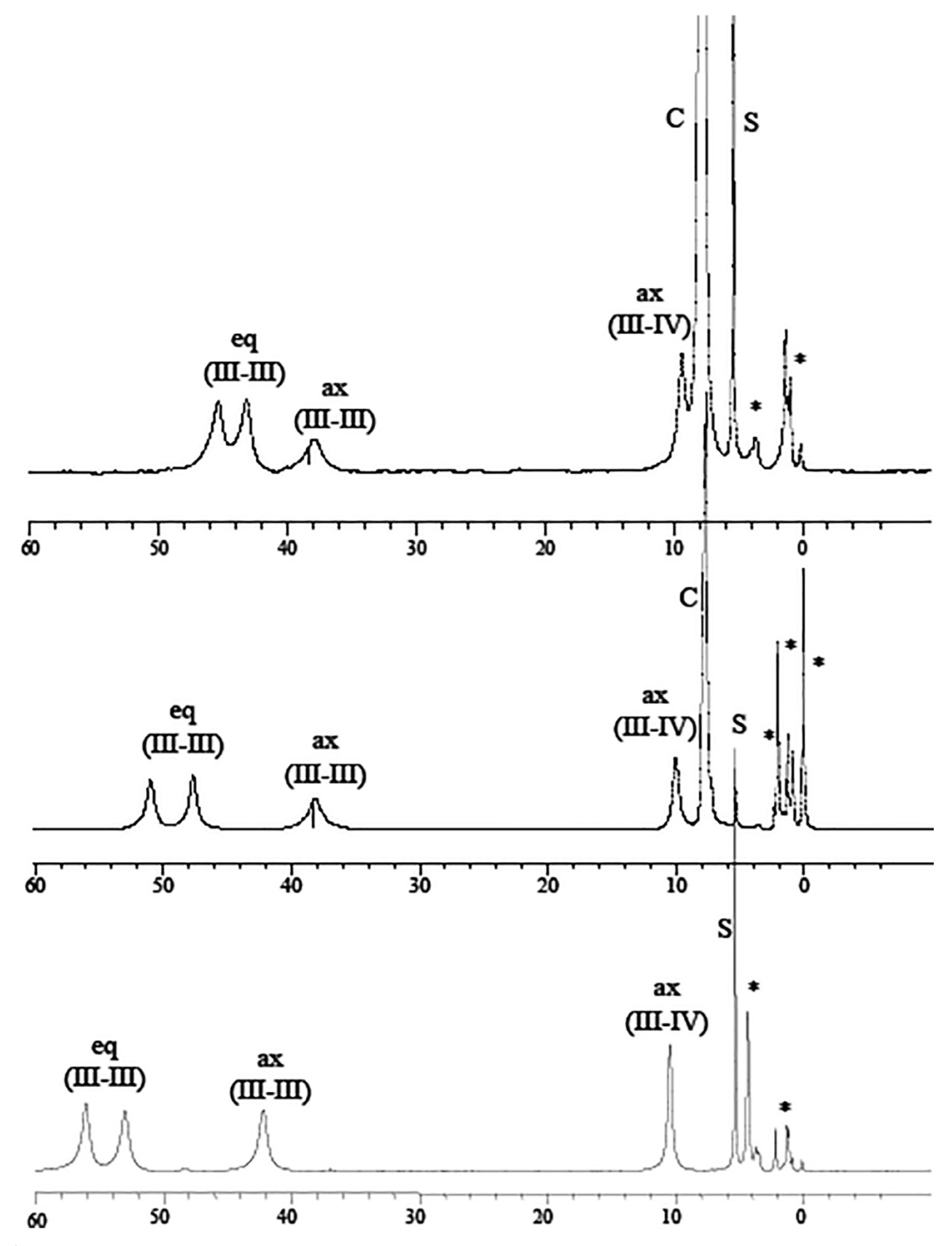


Fig. 5. 1 H NMR spectra in CD₂Cl₂ at ~23 $^{\circ}$ C of dried **3** (bottom), **6** (middle) and **8** (top). Peaks marked with * are solvent impurities (mainly hexane and water), S indicates solvent protio-impurity, and C are PPh₄ peaks; ax = axial, eq = equatorial.

Table 2 1 H NMR spectral data for $[Mn_{12}O_{12}(O_{2}CR)_{16}(H_{2}O)_{x}]^{n-}$ complexes.

Compound	Peak (ppm) ^a	Assignment ^b	$T_1(ms)$
$n = 0, R = Me(1)^{c}$	48.2	ax (III-III)	3.3
	41.8	eq (III-III)	3.4
	13.9	ax (III-IV	5.7
$n = 0, R = CH_2Cl (3)^d$	56	eq (III-III)	3.3
	53.1	eq (III-III)	2.9
	42.2	ax (III-III)	2.2
	10.3	ax (III-IV)	4.7
$n = 1-, R = CH_2Cl (6)^d$	51.4	eq (III-III)	2
	47.9	eq (III-III)	1.9
	39	ax (III-III)	1.8
	10	ax (III-IV)	4.5
$n = 2-, R = CH_2Cl(8)^d$	45.2	eq (III-III)	2
	42.9	eq (III-III)	1.8
	39.8	ax (III-III)	1.3
	9.3	ax (III-IV)	4.2

^a at ~ 23 °C. ^b ax = axial, eq = equatorial; III-III and III-IV refer to the ligands bridging Mn³⁺Mn³⁺ and Mn³⁺Mn⁴⁺ pairs, respectively. ^c in CD₂CN. ^d in CD₂Cl₂.

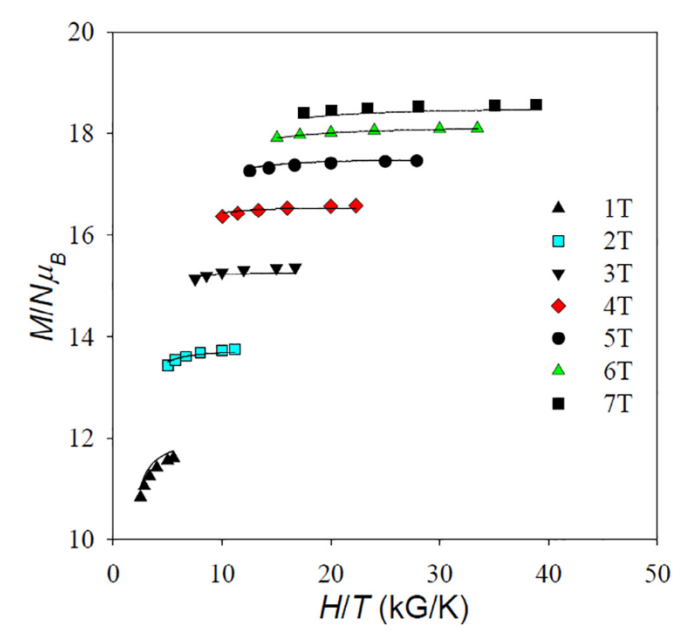


Fig. 6. Plot of reduced magnetization $(M/N\mu_B)$ vs. H/T data for complex **8**- $2H_2O$ at the indicated applied fields. The solid lines are the fit of the data; see the text for the fit parameters.

3.7. μ -SQUID studies on (PPh₄)[Mn₁₂O₁₂(O₂CCHCl₂)₁₆(H₂O)₄] **(5)** and (PPh₄)₂[Mn₁₂O₁₂(O₂CCH₂Cl)₁₆(H₂O)₃] **(8)**

Magnetization vs dc field scans were performed on aligned single crystals of $\mathbf{5}\cdot \mathbf{x}(\text{solv})$ and $\mathbf{8}\cdot \text{5CH}_2\text{Cl}_2\cdot \text{H}_2\text{O}$ freshly removed from mother liquor. For $\mathbf{8}\cdot \text{5CH}_2\text{Cl}_2\cdot \text{H}_2\text{O}$ the observed hysteresis loops at 0.004 T/s are shown in Fig. 10. Those in the 0.04–2.0 K range (Fig. 10, top) clearly show the temperature-dependent coercivity and quantum tunneling of magnetization (QTM) steps of a SMM, but also the presence of two species in the crystal, a faster-relaxing (FR) one and a slower-relaxing (SR) one in a ~90:10% ratio. Studies at ≤ 1.2 K allowed the study of the majority FR species with a smaller relaxation barrier ($\mathbf{8a}$) since the slower relaxing one with the larger barrier is completely blocked at these temperatures. The resulting hysteresis loops for $\mathbf{8a}$ are shown in Fig. 10, bottom.

Accurate measurement of the QTM step positions, determined from the first derivative of the hysteresis loops, gives the field separation between steps (ΔH), which allows the D parameter to be calculated using Eq. 5. An average ΔH of 0.19 T (1.9 kG) was obtained for **8a**, from which

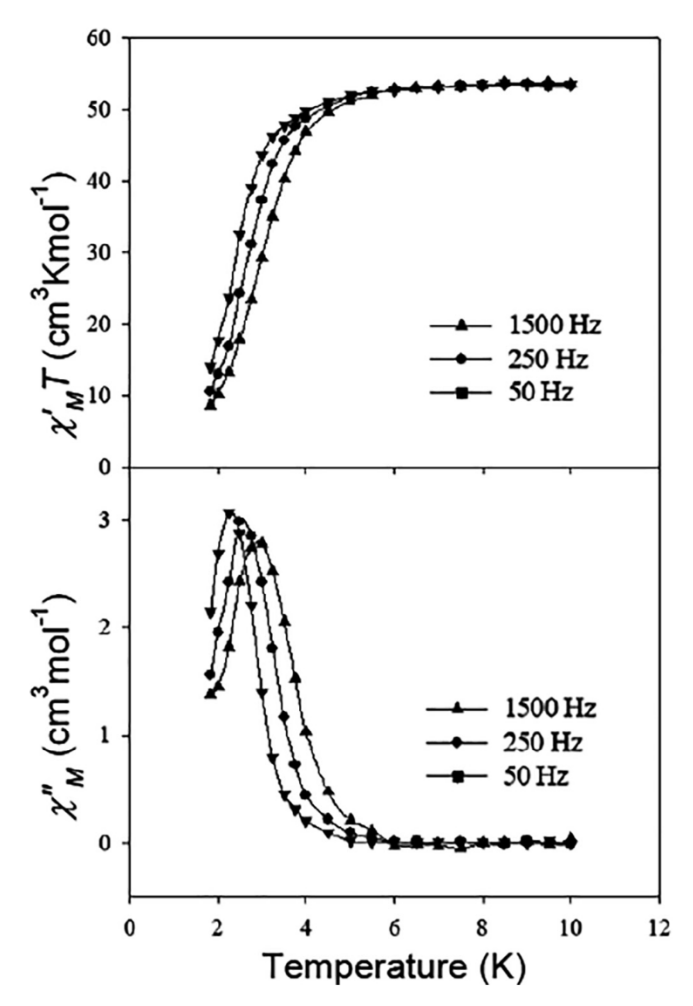


Fig. 7. In-phase $(\chi'_M$, as $\chi'_M T)$ vs T (top) and out-of-phase (χ''_M) vs T (bottom) ac susceptibility signals for vacuum-dried **8**·2H₂O at the indicated frequencies.

$$\Delta H = |D|/g\mu_{\rm B} \tag{5}$$

was calculated |D|/g = 0.088 cm⁻¹, which for $g \approx 2.0$ gives $D = -0.18 \text{ cm}^{-1} = -0.26 \text{ K}$. To determine U_{eff} , magnetization decay vs time data (Fig. S4) were collected for 8a using the method described elsewhere [34]. From these were obtained relaxation rate $(1/\tau)$ vs T data, where τ is the relaxation time, which are plotted as τ vs 1/T in green in Fig. 11. The fit of the thermally activated region to Eq. 4 (dashed line) gave $U_{\rm eff}$ = 21.6 K and τ_0 = 9.8 \times 10⁻⁹ s for **8a**. For comparison, also shown in red are the data and fit obtained from ac susceptibility data for the vacuum-dried sample as described above that gave $U_{\rm eff}$ = 33 K and τ_0 = 2.2 \times 10⁻⁹ s. Clearly there is a significant difference, and we assign this to the fact that the single-crystal μ -SQUID and ac χ''_{M} vs T studies were carried out on pristine 8.5CH₂Cl₂·H₂O vs vacuum-dried 8.2H₂O, respectively, pointing to significant changes caused by the drying. It was for this reason we collected the χ''_{M} vs T data on 8.5CH₂Cl₂·H₂O (Fig. 9), which showed that it is **FR** (smaller U_{eff}) than **8**·2H₂O, in agreement with the hysteresis results, and showed a shoulder at higher T likely corresponding to the small fraction of the SR higher-barrier component. This also explains why the Arrhenius plot (Fig. 11) has a discontinuity.

The behavior is reminiscent of the two forms of the R = CHCl₂ analogue, **10**·4CH₂Cl₂·H₂O and **10**·6CH₂Cl₂ reported elsewhere [34] with $U_{\rm eff}$ = 18.5 K and τ_0 = 5.3 × 10⁻⁸ s and $U_{\rm eff}$ = 30.3 K and τ_0 = 3.2 × 10⁻⁸ s, respectively. These, however, crystallized separately as a mixture of two crystal forms, thin plates and

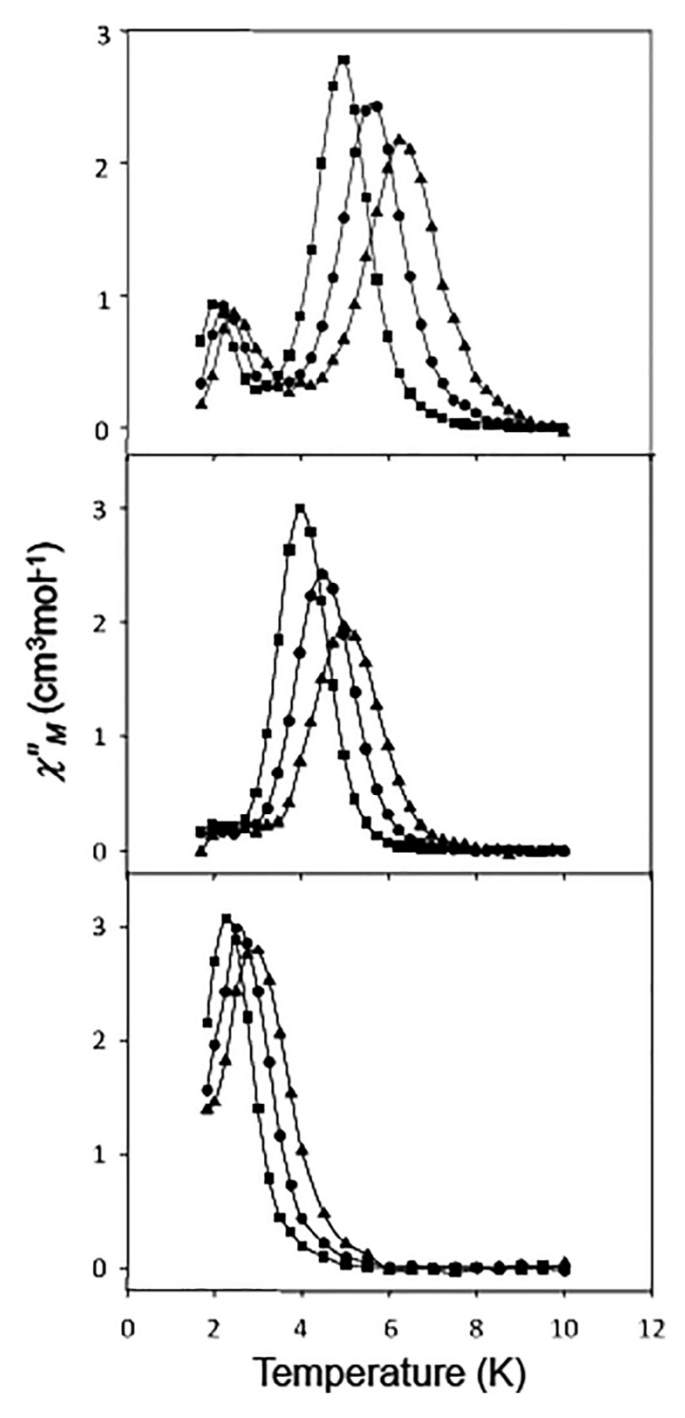


Fig. 8. χ''_M vs T plots at the indicated frequencies for the $[Mn_{12}O_{12}(O_2CCH_2CI)_{16}(H_2O)_x]^n$ family as vacuum-dried solids: (a) **3** (n = 0, x = 4); (b) **6**·H₂O (n = 1-, x = 4); and (c) **8**·2H₂O (n = 2-, x = 3).

needles, respectively, allowing convenient μ -SQUID study of individual crystals of each complex. Both forms of **10** are normal JT isomers, as is **8**·5CH₂Cl₂·H₂O, so the different $U_{\rm eff}$ in the latter is again assigned to subtle environmental differences in the two forms owing to the presence of so much solvent. Interestingly, both **FR 10**·4CH₂Cl₂·H₂O and **8**·5CH₂Cl₂·H₂O have their lattice H₂O molecule hydrogen-bonding with a cubane O²⁻ ion in the core, contributing to lowering of the core symmetry, as does five-coordinate Mn10 in the latter complex, and leading to it being **FR** as a result. Vacuum-drying removes all CH₂Cl₂ solvent molecules in the two forms of **10** giving $U_{\rm eff}$ = 32 K and τ_0 = 3.1 × 10⁻⁹ s, closer to the **SR** form. Similarly, vacuum-dried **8**·2H₂O gives similar values of $U_{\rm eff}$ = 33 K and τ_0 = 2.2 × 10⁻⁹ s.

For $5 \cdot x$ (solv), we have already reported the magnetic properties of vaccum-dried $5.^3/_2$ hexane [32] and shown that it exhibits a χ''_M peak in the 4-6 K range (Fig. S5b). With the present results on the pristine 8.5CH₂Cl₂·H₂O vs vacuum-dried 8.2H₂O differences, we have gone back to probe whether 5 shows similar behavior. Indeed, pristine $\mathbf{5} \cdot \mathbf{x}(\text{solv})$ gives three sets of χ''_{M} vs T signals, in the <2 K (5a), 2 – 4 K (5b), and 4–6 K (5c) ranges (Fig. 12). A single-crystal μ-SQUID study indicated that all forms are present in the crystal, as seen for 8.5CH2Cl2·H2O rather than 10 and, upon vacuum-drying, the two **FR** forms convert to a **SR** form with χ''_M signals in the 4–6 K range. This was the reason we obtained the crystal structure, wondering whether we might provide evidence in this case of IT isomerism or whether the multiple forms were again just due to solvent-based environmental differences. However, the high-symmetry cubic I43m space group with only $\frac{1}{8}$ of the $[Mn_{12}]^-$ anion in the asymmetric unit masks any differences due to IT isomerism that might be present. We did try to grow crystals in a lower symmetry space group but the only ones obtained of sufficient quality were also I43m and the structure was not pursued: 5.2hexane, cubic, I43m, a = b = c = 29.3518(12), $\alpha = \beta = \gamma = 90^{\circ}$.

The $I\!\!A3m$ space group means three mutually perpendicular orientations of the clusters, and therefore the dc field could only be applied parallel to the easy- (z-) axes of $^1/_3$ of the molecules for the hysteresis studies; thus its perpendicular alignment to the other $^2/_3$ of the clusters represents a transverse field explaining the broad nature and ill-defined features of the hysteresis loops. Nevertheless, judicious control of temperature allowed magnetization vs time decay data to be collected on all three forms (Fig. S7), from which the Arrhenius plots of Fig. 13 were constructed.

Fits of the thermally-activated regions gave: $U_{\rm eff} = 15$ K and $\tau_0 = 1.1 \times 10^{-7}$ s for **5a**; $U_{\rm eff} = 31$ K and $\tau_0 = 5.3 \times 10^{-9}$ s for **5b**; and $U_{\rm eff} = 53$ K and $\tau_0 = 7.1 \times 10^{-9}$ s for **5c**. As stated above, vacuum-dried **5**· $^3/_2$ hexane then gives essentially a single **FR** species, with $U_{\rm eff} = 57$ K and $\tau_0 = 1.7 \times 10^{-9}$ s. The overall behavior of pristine **5**·x(solv) thus parallels those of **8** and **10**, i.e., multiple forms in the pristine crystals all collapsing on vacuum drying to a **SR** form. The $U_{\rm eff} = 57$ K of **5**· $^3/_2$ (hexane) is similar to the $U_{\rm eff} = 53$ K of the **SR 5c** in the pristine crystal. Since the upper limit of the relaxation barrier is given by $U = (S^2 - 1/_4)|D|$, and remembering that $U_{\rm eff} < U$

Table 3 Comparison of magnetic data^a for $[Mn_{12}O_{12}(O_2CR)_{16}(H_2O)_4]^{2-}$ complexes.

Parameter	CH ₂ CI (8)	CHCl ₂ (10)	C ₆ F ₅ (11)	$C_6H_3(NO_2)_2$ (9)
S	10	10	10	10
g ^c	1.94	2.00	2.01	1.94
D , cm $^{-1}$ a,d	-0.26	-0.27	-0.28	-0.28
D, K ^{a,d}	-0.37	-0.39	-0.40	-0.40
U, K ^{a,d,e}	37	39	40	40
U _{eff} , K ^{a,d} U _{eff} , K ^{b,d}	33	32	31	31
U _{eff} , K ^{b,d}	22	19, 30	25 ^f	n/a

^aFor vacuum-dried microcrystals. ^bFor wet single crystal. ^c ±0.02. ^d ±0.2 ^e calculated by $U = S^2 |D|$. ^fCombined dc and ac data. n/a = not available.

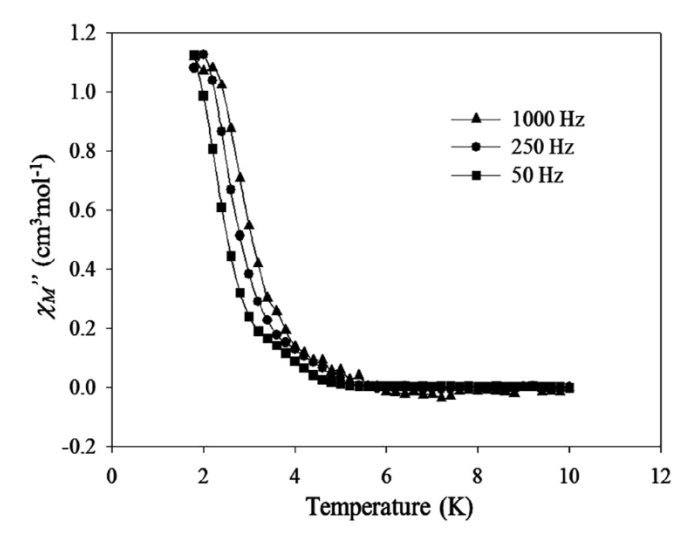


Fig. 9. χ''_{M} vs T plots at the indicated frequencies for **8**-5CH₂Cl₂·H₂O freshly taken from mother liquor, dabbed dry with tissue, and enveloped in eicosane for study.

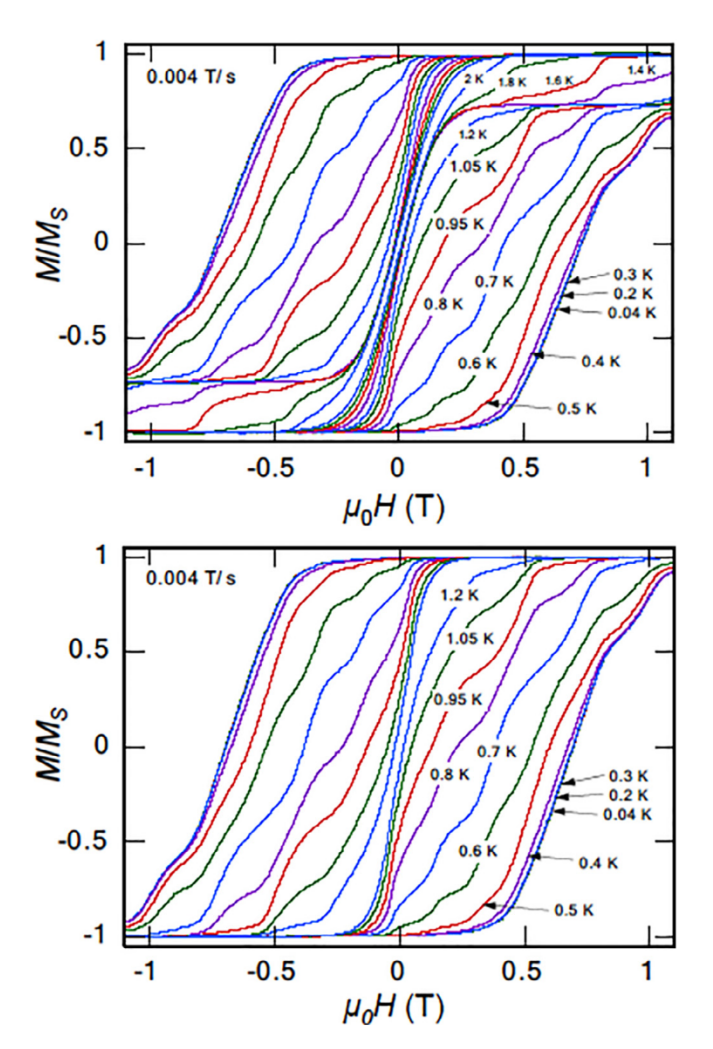


Fig. 10. Magnetization vs dc field hysteresis loops at a 0.004 T/s field sweep rate for a single crystal of $8.5\text{CH}_2\text{Cl}_2\cdot\text{H}_2\text{O}$: (top) in the 0.04–2.0 K range to show features from both species present, and (bottom) in the 0.04–1.2 K range to show features just from the majority species 8a. The magnetization is normalized to its saturation value, M_5 .

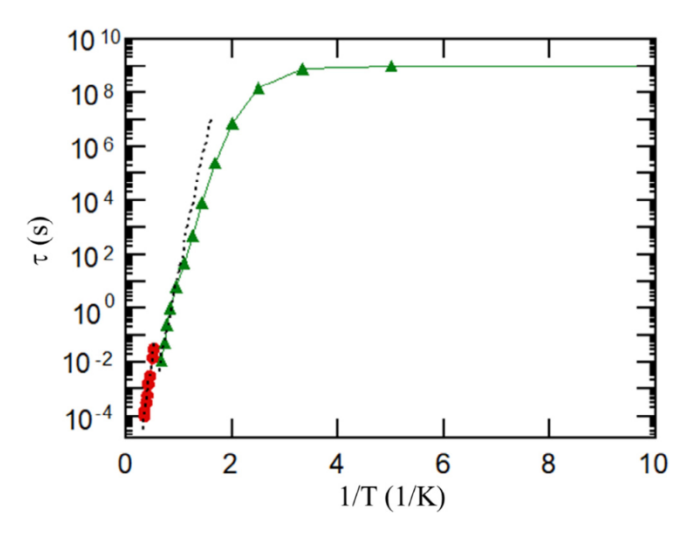


Fig. 11. τ vs 1/T Arrhenius plot for **8a** in a single crystal of **8**·5CH₂Cl₂·H₂O (\triangle) using data from the magnetization vs time decay study, and showing the relaxation becoming *T*-independent below 0.4 K; the green line is a guide for the eyes. Also shown are the corresponding data (\bigcirc) obtained at higher *T* from ac susceptibility measurements on vacuum-dried **8**··2H₂O. The dashed lines are the fits in each case to the Arrhenius equation. See the text for the fit parameters.

due to QTM, this would suggest a minimum value of $|D| \approx 0.41$ and 0.44 cm⁻¹ for **5c** and $5.^3/_2$ (hexane), respectively. To probe this more accurately, we carried out high-frequency EPR (HFEPR) studies of $5.^3/_2$ (hexane).

3.8. High-field electron paramagnetic resonance (HFEPR) spectroscopy on $\mathbf{5}^{-3}/_{2}$ hexane

HFEPR measurements were performed on a finely ground powder sample of $5^{.3}/2$ hexane as a function of both frequency and temperature; representative spectra are shown along with simulations in Fig. 14. In the displayed field range, the powder spectra are dominated by crystallites that have their z-axes parallel to the applied magnetic field, with resonances appearing as peaks in the dI/dB signal; these resonances are labeled z_i in Fig. 14, where i=1, 2, 3, etc. The ground-state transition (z_1) can be identified from the temperature-dependence (Fig. 14b), as it is the strongest resonance at the lowest temperature. An initial estimate of the axial zfs parameter, D, can be obtained by plotting the positions of the resonances on a 2D frequency vs field plot (Fig. S8). On the basis of Eq. (3), a linear fit to the z_1 resonance yields an intercept on the frequency axis of 18D (=250 GHz) for a molecule with a ground state spin of $S = {}^{19}/{}_2$ (see SI).

Spectral simulations (Fig. 14) were subsequently performed using the program EasySpin [60], with the initial estimate of D as a starting point. In order to achieve the best simulations, it was necessary to add an axial fourth order zfs term to Eq. (3) of the form, $B_4^0 \widehat{O}_4^0$, where \widehat{O}_4^0 is an extended Stevens operator [60] and B_4^0 the associated zfs parameter. This 4th order interaction is well documented in polynuclear SMMs with low-lying excited states [61,62,63], including essentially all Mn₁₂ species [64,65]. A combination of Gaussian line broadening (0.4 T peak-to-peak) and a slight ordering of the powder sample was also needed in order to obtain a satisfactory correspondence between the experimental spectra and the simulations. The ordering implies that the magnetic torque on the microcrystals in the powder caused a preferential alignment of the magnetic easy- (z-) axes with the applied field. The best overall simulations of the combined temperature and frequency dependent HFEPR measurements were obtained

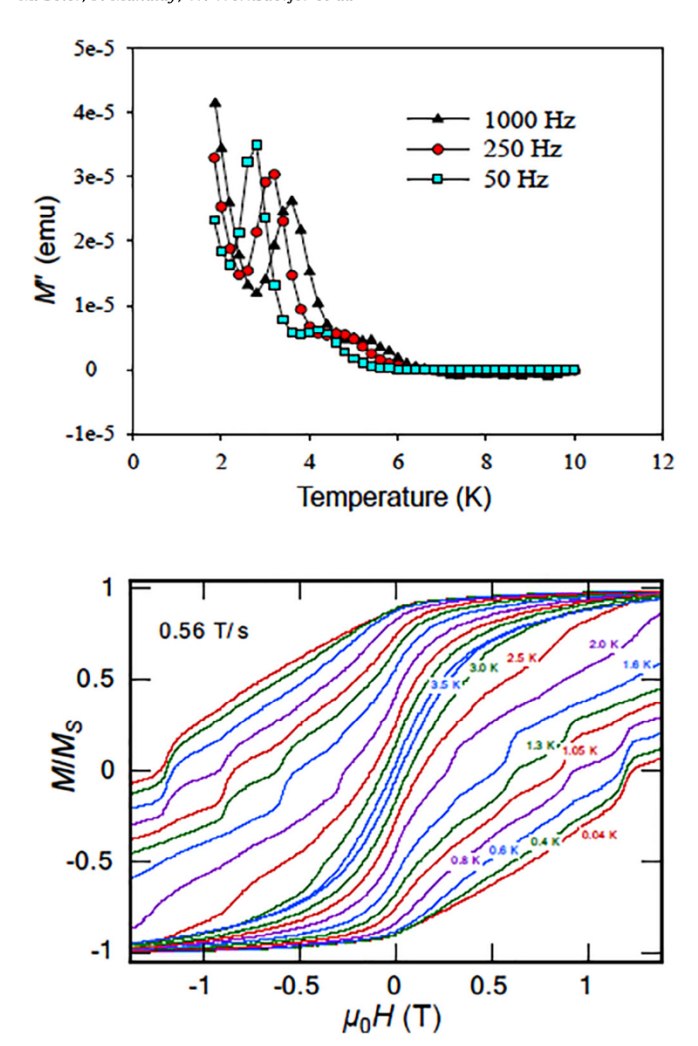


Fig. 12. (top) Ac out-of-phase magnetization M'' vs T plots at the indicated frequencies for $\mathbf{5}$ -x(solv) freshly taken from mother liquor, dabbed dry with tissue, and enveloped in eicosane for study. **(bottom)** Magnetization vs dc field hysteresis loops at a 0.56 T/s field sweep rate for a single crystal of $\mathbf{5}$ -x(solv) in the 0.04–3.5 K range to show features from the three species $\mathbf{5a}$ - \mathbf{c} present. The magnetization is normalized to its saturation value, $M_{\rm S}$.

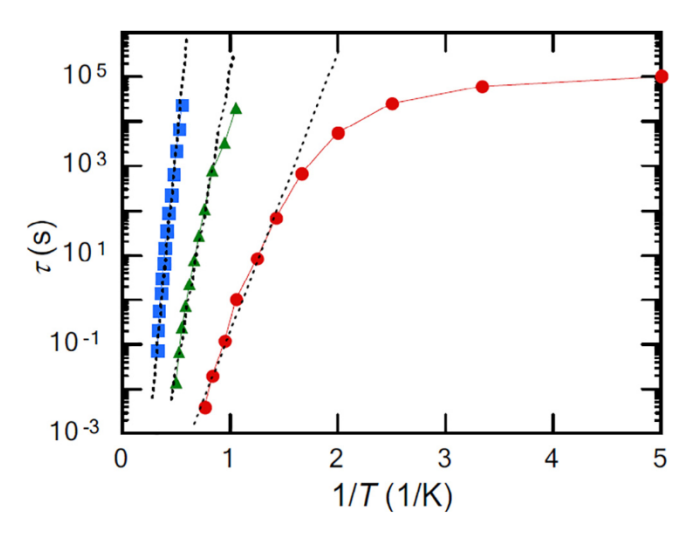


Fig. 13. τ vs 1/T Arrhenius plots for 5a (\bigcirc), 5b (\bigcirc), and 5c (\bigcirc) in a single crystal of $5 \cdot x$ (solv) using data from the magnetization vs time decay study, and showing the relaxation for 5a becoming T-independent below ~ 0.3 K; the solid colored lines are guides for the eyes. The dashed lines are the fits in each case to the Arrhenius equation. See the text for the fit parameters.

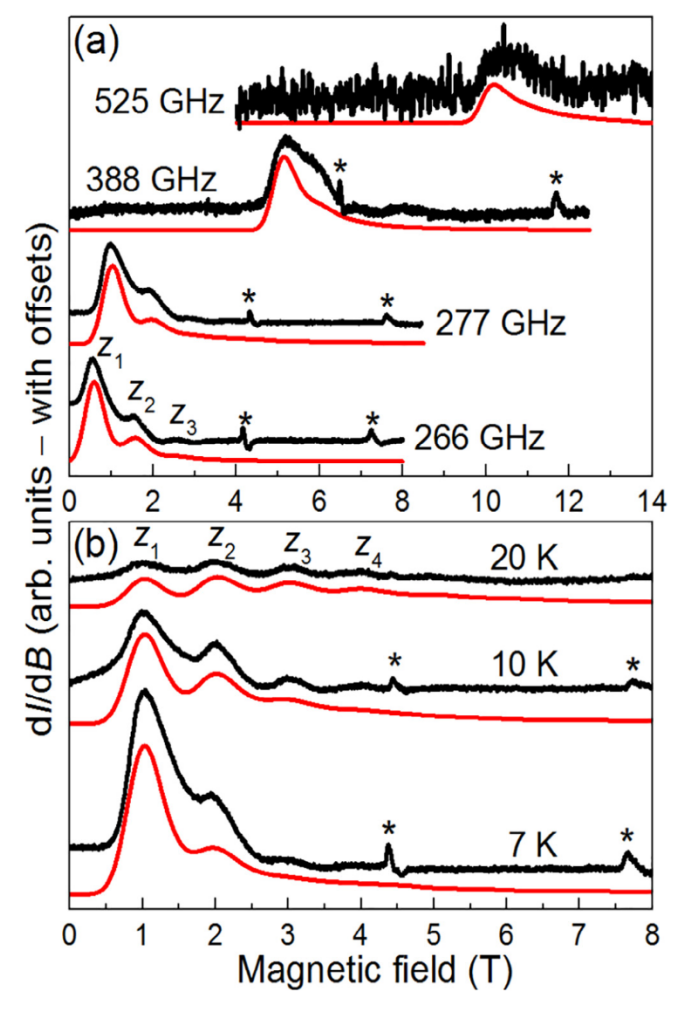


Fig. 14. (a) Frequency-dependent HFEPR spectra (black) for a vacuum-dried polycrystalline powder sample of $5.^3/_2$ hexane at T=7 K. (b) Temperature dependence of the 277.1 GHz spectrum in (a). Simulations (red) are shown below each experimental trace in both (a) and (b); see text for obtained z sparameters. Up to four resonances can be identified that are associated with the parallel (H/|z) component of the full spectrum; these are labeled z_1 to z_4 , corresponding to the $m_S = -\frac{19}{2} \rightarrow -\frac{17}{2} \rightarrow -\frac{15}{2} \rightarrow -\frac{15}{2} \rightarrow -\frac{13}{2} \rightarrow -\frac{13}{2}$, and $-\frac{13}{2} \rightarrow -\frac{11}{2}$ transitions (see Fig. S8). Features marked with an asterisk are due to a known frozen molecular oxygen contaminant in the sample holder.

with the following spin Hamiltonian parameters: $S = {}^{19}/_2$, $g_z = 1.96$ (2), D = -0.477 cm⁻¹ and $B_4^0 = +3.3(2) \times 10^{-6}$ cm⁻¹.

The strongest parallel $(z_i, i \le 4)$ resonances are insensitive to the x and y components of the g-tensor as well as any off-diagonal zfs terms, such as the rhombic anisotropy $E(\widehat{S}_x^2 - \widehat{S}_y^2)$. Consequently, these parameters $(g_x, g_y \text{ and } E)$ remain undetermined, in part due to the sample ordering, but also because the strongest perpendicular (B//xy) resonances occur beyond the maximum available field for the high frequencies employed in this study. However, the HFEPR studies nevertheless confirm the sizeable Dvalue for $\mathbf{5}^{3}/_{2}$ hexane. Fits of magnetization vs. field data for $[Mn_{12}]^-$ clusters collected at low T typically give smaller values of |D| in the range 0.3 – 0.4 cm⁻¹ [26,33]. However, the values determined from HFEPR are more reliably accurate. More importantly, the axial zfs parameters obtained from the HFEPR measurements on 5.3/2 hexane result in a theoretical barrier of U = 62 K, rationalizing the experimentally determined $U_{\rm eff}$ = 57 K from ac data. As stated above, the slight reduction of U_{eff} relative to U is likely due to under-barrier QTM [59].

4. Conclusions

The family of reduced $[Mn_{12}O_{12}(O_2CR)_{16}(H_2O)_x]^{n-}$ complexes has been expanded in this work, and conclusions deduced in the past on the basis of a smaller number of examples have in general been supported, such as reduction taking place at outer Mn³⁺ rather than inner Mn^{4+} ions, and the two Mn^{2+} ions in $[Mn_{12}]^{2-}$ species adopting trans locations in the cluster. Of particular interest in the present work has been the identification in 8.5CH₂Cl₂·H₂-O of two forms with different $U_{\rm eff}$ values, similar to those in 10 which crystallized separately, and which we thus also assign as likely due to environmental effects of the lattice solvent molecules rather than the JT isomerism identified in neutral Mn_{12} molecules. Thus, when the solvent molecules are removed, the clusters relax to their SR form, which is also the case for JT isomers. Extending this to $\mathbf{5} \cdot \mathbf{x}(\text{solv})$ showed three forms to be present in the pristine crystal, with one having a $U_{\rm eff}$ of only 15 K, remarkably small for a [Mn₁₂]⁻ species. We are intrigued that this unusual situation might indeed involve JT isomerism but unfortunately the highsymmetry crystal structure does not allow us to make any firm conclusion on this point, and the latter must await lower-symmetry systems. A main conclusion of this work in addition to expanding this family of SMMs is thus the remarkable sensitivity of these ultra-small nanoscale magnets to their environment, as manifested in their properties, especially their quantum properties that are so important to the potential application of SMMs in a variety of new 21st century technologies.

Declaration of Competing Interest

The authors declare that they have no known competing financial interests or personal relationships that could have appeared to influence the work reported in this paper.

Acknowledgment

This work was supported by the Center for Molecular Magnetic Quantum Materials, an Energy Frontier Research Center funded by the U.S. Department of Energy, Office of Science, Basic Energy Sciences under Award No. DE-SC0019330. HFEPR measurements were performed using instruments at the National High Magnetic Field Laboratory, which is supported by the National Science Foundation (DMR-1644779) and the State of Florida. We thank the NSF for funding of the X-ray diffractometer through grant CHE-1828064, and Maren Pink of the Molecular Structure Center, Indiana University, Bloomington, for additional refinement of the structure of **8**•5CH₂Cl₂•H₂O.

Appendix A. Supplementary data

Supplementary data to this article can be found online at https://doi.org/10.1016/j.poly.2020.114968.

References

- [1] T. Lis, Acta. Crystallogr. Sect. B: Struc. Sci. 36 (1980) 2042.
- [2] P.S. Perlepes, D. Maniaki, E. Pilichos, E. Katsoulakou, S.P. Perlepes, Inorganics 8 (2020) 39.
- [3] R.A. Layfield, Organometallics 33 (2014) 1084-1099.
- [4] D.N. Woodruff, R.E.P. Winpenny, R.A. Layfield, Chem. Rev. 113 (2013) 5110–5148.
- [5] G.A. Craig, M. Murrie, Chem. Soc. Rev. 44 (2015) 2135-2147.
- [6] P.L. Feng, C. Koo, J.J. Henderson, M. Nakano, S. Hill, E. del Barco, D.N. Hendrickson, Inorg. Chem. 47 (2008) 8610–8612.
- [7] R. Inglis, S.M. Taylor, L.F. Jones, G.S. Papaefstathiou, S.P. Perlepes, S. Datta, S. Hill, W. Wernsdorfer, E.K. Brechin, Dalton Trans. (2009) 9157–9168.
- [8] T.C. Stamatatos, D. Foguet-Albiol, C.C. Stoumpos, C.P. Raptopoulou, A. Terzis, W. Wernsdorfer, S.P. Perlepes, G. Christou, J. Am. Chem. Soc. 127 (2005) 15380–15381.

- [9] C.-I. Yang, W. Wernsdorfer, K.-H. Cheng, M. Nakano, G.-H. Lee, H.-L. Tsai, Inorg. Chem. 47 (2008) 10184–10186.
- [10] A.J. Tasiopoulos, A. Vinslava, W. Wernsdorfer, K.A. Abboud, G. Christou, Angew. Chem. Int, Ed. 116 (2004) 2169–2173.
- [11] G. Aromi, E.K. Brechin, Single-molecule Magnets and Related Phenomena, Springer, 2006, pp. 1–67.
- [12] R. Clérac, Angew. Chem. Int. Ed. 51 (2012) 7079-7080.
- [13] K.R. Meihaus, J.R. Long, Dalton Trans. 44 (2015) 2517–2528.
- [14] L.R. Piquer, E.C. Sañudo, Dalton Trans. 44 (2015) 8771-8780.
- [15] M. Sakamoto, K. Manseki, H. Okawa, Coord. Chem. Rev. 219–221 (2001) 379–414.
- [16] C. Benelli, D. Gatteschi, Chem. Rev. 102 (2002) 2369-2387.
- [17] C.A.P. Goodwin, F. Ortu, D. Reta, N.F. Chilton, D.P. Mills, Nature 548 (2017) 439–442
- [18] (a) F.-S. Guo, B.M. Day, Y.-C. Chen, M.-L. Tong, A. Mansikkamaki, R.A. Layfield, Angew. Chem. Int. Ed. 56 (2017) 1–6; (b) F.-S. Guo, B.M. Day, Y.-C. Chen, M.-L. Tong, A. Mansikkamaki, R.A. Layfield, Science 362 (2018) 1400–1403.
- [19] J.R. Friedman, M. Sarachik, J. Tejada, R. Ziolo, Phys. Rev. Lett. 76 (1996) 3830.
- [20] L. Thomas, F. Lionti, R. Ballou, D. Gatteschi, R. Sessoli, B. Barbara, Nature 383 (1996) 145–147.
- [21] W. Wernsdorfer, N. Chakov, G. Christou, Phys. Rev. Lett. 95 (2005).
- [22] W. Wernsdorfer, R. Sessoli, Science 284 (1999) 133-135.
- [23] W. Wernsdorfer, M. Soler, G. Christou, D. Hendrickson, J. Appl. Phys. 91 (2002) 7164–7166.
- [24] (a) S. Hill, R. S. Edwards, N. Aliaga-Alcalde and G. Christou, Science, 302 (2003) 1015-1018. (b) R. Tiron, W. Wernsdorfer, D. Foguet-Albiol, N. Aliaga-Alcalde, and G. Christou, Phys. Rev. Lett. 91 (2003) 227203(1-4).
- [25] T.N. Nguyen, W. Wernsdorfer, K.A. Abboud, G. Christou, J. Am. Chem. Soc. 133 (2011) 20688–20691.
- [26] W. Wernsdorfer, N. Aliaga-Alcalde, D.N. Hendrickson, G. Christou, Nature 416 (2002) 406–409.
- [27] W. Wernsdorfer, N. Aliaga-Alcalde, R. Tiron, D. Hendrickson, G. Christou, J. Mag. Magnet. Mater. 272 (2004) 1037–1041.
- [28] R. Bagai, G. Christou, Chem. Soc. Rev. 38 (2009) 1011-1026.
- [29] R. Sessoli, H.-L. Tsai, A.R. Schake, S. Wang, J.B. Vincent, K. Folting, D. Gatteschi, G. Christou, D.N. Hendrickson, J. Am. Chem. Soc. 115 (1993) 1804–1816.
- [30] H.J. Eppley, H.-L. Tsai, N. de Vries, K. Folting, G. Christou, D.N. Hendrickson, J Am. Chem. Soc. 117 (1995) 301–317.
- [31] S.M. Aubin, Z. Sun, H.J. Eppley, E.M. Rumberger, I.A. Guzei, K. Folting, P.K. Gantzel, A.L. Rheingold, G. Christou, D.N. Hendrickson, Inorg. Chem. 40 (2001) 2127–2146.
- [32] Z.M. Sun, D. Ruiz, N.R. Dilley, M. Soler, J. Ribas, K. Folting, M.B. Maple, G. Christou, D.N. Hendrickson, Chem. Commun. (1999, 1973.).
- [33] M. Soler, W. Wernsdorfer, Z.M. Sun, J.C. Huffman, D.N. Hendrickson, G. Christou, Chem. Commun. (2003) 2672.
- [34] M. Soler, W. Wernsdorfer, K.A. Abboud, J.C. Huffman, E.R. Davidson, D.N. Hendrickson, G. Christou, J. Am. Chem. Soc. 125 (2003) 3576–3588.
- [35] N.E. Chakov, M. Soler, W. Wernsdorfer, K.A. Abboud, G. Christou, Inorg. Chem. 44 (2005) 5304–5321.
- [36] H.-L. Tsai, H.-A. Shiao, T.-Y. Jwo, C.-I. Yang, C.-S. Wur, G.-H. Lee, Polyhedron 24 (2005) 2205–2214.
- [37] F. Moro, R. Biagi, V. Corradini, M. Evangelisti, A. Gambardella, V.D. Renzi, U. del Pennino, E. Coronado, A. Forment-Aliaga, F.M. Romero, J. Phys. Chem. C. 116 (2012) 14936–14942.
- [38] M. Soler, P. Artus, K. Folting, J.C. Huffman, D.N. Hendrickson, G. Christou, Inorg. Chem. 40 (2001) 4902–4912.
- [39] M. Soler, S.K. Chandra, D. Ruiz, J.C. Huffman, D.N. Hendrickson, G. Christou, Polyhedron 20 (2001) 1279–1283.
- [40] SHELXTL, in, Bruker AXS Inc.: Madison, Wisconsin, USA, 2014.
- [41] SHELXS-97, Bruker-AXS, Madison, WI, USA (1997).
- [42] P. Squeeze, Acta Cryst. A 46 (1990) 194-201.
- [43] A.L. Spek, PLATON, Acta Cryst. A46 (1990) C-34.
- [44] E. Davidson, MAGNET, Indiana University, Bloomington, IN, 1999.
- [45] R.C. Weast, M.J. Astle, CRC Handbook of Chemistry and Physics, CRC Press Inc., Boca Raton, FL, 1983.
- [46] W. Wernsdorfer, Adv. Chem. Phys. 118 (2001) 99.
- [47] A. Hassan, L. Pardi, J. Krzystek, A. Sienkiewicz, P. Goy, M. Rohrer, L.-C. Brunel, J. Magn. Reson. 142 (2000) 300.
- [48] (a) P. Maruthamuthu, R.E. Huie, Chemosphere 30 (1995) 2199–2207;
 (b) G. Smith, R.C. Bott, U.D. Wermuth, Acta. Crystallogr. Sect. C.: Cryst. Struc. Commun. 56 (2000) 1505–1506;
 (c) E.P. Serjeant, B. Dempsey, Ionisation Constants of Organic Acids in Aqueous Solution. IUPAC Chemical Data Series Number 23, Pergamon Press, New York,
- NY, 1979, p. 26.
 [49] J.M. Clemente-Juan, E. Coronado, A. Forment-Aliaga, A. Gaita-Arino, C. Giménez-Saiz, F.M. Romero, W. Wernsdorfer, R. Biagi, V. Corradini, Inorg. Chem. 49 (2010) 386–396.
- [50] H. Wang, S. Hamanaka, T. Yokoyama, H. Yoshikawa, K. Awaga, Chem. Asian. J. 6 (2011) 1074–1079.
- [51] M. Soler, S.K. Chandra, D. Ruiz, E.R. Davidson, D.N. Hendrickson, G. Christou, Chem. Commun. (2000) 2417–2418.
- [52] I. Brown, D. Altermatt, Acta. Crystallogr. Sect. B: Struct. Sci. 41 (1985) 244–247.
- [53] A.W. Addison, T.N. Rao, J. Reedijk, J. van Rijn, G.C. Verschoor, J. Chem. Soc., Dalton Trans. (1984) 1349–1356.
- [54] E.T. Muetterties, L. Guggenberger, J. Am. Chem. Soc. 96 (1974) 1748–1756.

- [55] S. Alvarez, M. Llunell, J. Chem. Soc., Dalton Trans. (2000) 3288–3303.
- [56] M. Chan, W. Armstrong, J. Am. Chem. Soc. 112 (1990) 4985–4986.
- [57] Z. Sun, P.K. Gantzel, D.N. Hendrickson, Inorg. Chem. 35 (1996) 6640–6641.
- [58] T. Kuroda-Sowa, G.-Q. Bian, M. Hatano, H. Konaka, S. Fukuda, S. Miyoshi, M. Maekawa, M. Munakata, H. Miyasaka, M. Yamashita, Polyhedron 24 (2005) 2680-2690.
- [59] S. Hill, M. Murugesu, G. Christou, Phys. Rev. B 80 (2009) 174416.
 [60] S. Stoll, A. Schweiger, J. Magn. Reson. 178 (2006) 42–55.

- [61] A. Wilson, J. Lawrence, E.-C. Yang, M. Nakano, D.N. Hendrickson, S. Hill, Phys.
- [62] S. Hill, S. Datta, J. Liu, R. Inglis, C.J. Milios, P.L. Feng, J.J. Henderson, E. del Barco, E.K. Brechin, D.N. Hendrickson, Dalton Trans. 39 (2010) 4693–4707.
 [63] J. Marbey, P.-R. Gan, E.-C. Yang, S. Hill, Phys. Rev. B 98 (2018) 1444433.
 [64] C. Lampropoulos, M. Murugesu, A.G. Harter, W. Wernsdofer, S. Hill, N.S. Dalal, M. Marchell, M. S. Chill, Phys. Rev. B 98 (2018) 242000 (2018) 2420
- K.A. Abboud, G. Christou, Inorg. Chem. 52 (2013) 258-272.
- [65] S. Hill, Polyhedron 64 (2013) 128–135.